Cryo-EM Structure of an Active Bacterial SIR2-STAND Filament

Yiqun Wang[1], Yuqing Tian[1], Xu Yang[1], Feng Yu[1] and Jianting Zheng[1,2*]
[1]State Key Laboratory of Microbial Metabolism, School of Life Sciences and Biotechnology, Shanghai Jiao Tong University, Shanghai 200240, China
[2]Joint International Research Laboratory of Metabolic & Developmental Sciences, Shanghai Jiao Tong University, Shanghai 200240, China
[*]Correspondence: Jianting Zheng, E-mail: jtzheng@sjtu.edu.cn

Abstract

The signal transduction ATPases with numerous domains (STAND) superfamily encompasses widely distributed immune systems across bacteria, eukaryotes and archaea. The bacterial antiviral STAND type 5 (Avs5) contains an N-terminal Sirtuin (SIR2) domain, which protects against phage invasion. Despite the established roles of SIR2 and STAND in prokaryotic and eukaryotic immunity, the mechanism underlying their collaboration remains unclear. Here we present cryo-EM structures of *Escherichia fergusonii* Avs5 (*Ef*Avs5) filaments, elucidating the mechanisms of dimerization, filamentation, filament clustering, ATP binding and NAD^+ hydrolysis, all of which are crucial for anti-phage defense. The SIR2 domains and nucleotide-binding oligomerization domains (NOD) engage in the intra- and inter-dimer interaction to form an individual filament, while the outward C-terminal domains contribute to bundle formation. Filamentation potentially stabilizes the dimeric SIR2 configuration, thereby activating the NADase activity of *Ef*Avs5. *Ef*Avs5 is deficient in the ATPase activity, but elevated ATP concentrations can impede its NADase activity. Together, we uncover the filament assembly of Avs5 as a unique mechanism to switch enzyme activities and perform anti-phage defenses.

Keywords

Sirtuin, signal transduction ATPases with numerous domains, bacterial defense system, NAD^+ hydrolysis, filament formation

Keypoints

- *Ef*Avs5 depletes NAD^+ for anti-phage defense.
- *Ef*Avs5 assembles as bundled filaments that can hydrolyze NAD^+.
- The SIR2 domain and NOD collaborate to form an individual filament.
- The building block of the filament is *Ef*Avs5 dimer.
- The activity of the *Ef*Avs5 complex is regulated by ATP.

Introduction

Bacteria are in constant conflict with bacteriophages and develop diverse anti-phage defense systems of varying complexity[1-3]. The signal transduction ATPases with numerous domains (STAND) superfamily of P-loop NTPases recognizes pathogens and triggers downstream inflammatory responses or apoptotic processes through oligomerization, representing a conserved immune strategy in eukaryotes, exemplified by animal

inflammasomes and plant resistosomes[4-6]. Recently, this mechanism has also been discovered in the innate immunity of bacteria, known as antiviral STANDs (Avs)[3]. Avs proteins have a characteristic tripartite domain architecture: a central NTPase (alternatively called nucleotide-binding oligomerization domain, NOD); an extended C-terminal sensor with superstructure-forming repeats; and a variable N-terminal effector typically involved in cell death. Previous studies have revealed that Avs1-3 and Avs4 are activated by the phage terminases and portals, respectively, leading to the formation of tetramers that activate their N-terminal nucleases for antiviral defense[4].

Avs type 5 (Avs5) contains an N-terminal sirtuin (SIR2) effector and an unusual short C-terminal sensor domain, sometimes termed SIR2-STAND[3]. SIR2-mediated nicotinamide adenine dinucleotide hydrolase (NADase) activity represents a critical element in anti-phage immunity, triggering abortive infections via NAD^+ degradation and halting phage propagation, as exemplified by pAgo, Thoeris, DSR2, and the SIR2-HerA system[7-10]. In the Thoeris system, the signaling molecule 1"-3' gcADPR activates ThsA, which subsequently forms filaments and depletes NAD^+, ultimately triggering cell death and thereby preventing the spread of phage infection[11]. Another defense system DSR2 tetramerizes to form a supramolecular complex that specifically recognizes phage tail tube proteins, and leads to cellular NAD^+ depletion[12].

Despite reports on SIR2 and STAND roles in prokaryotic and eukaryotic immunity, the collaborative mechanism between them and the mechanisms underlying Avs5 activation and assembly remain obscure. Here, we present a biochemical and structural analysis of *Escherichia fergusonii* Avs5 (*Ef*Avs5), unveiling a unique mechanism of assembly-mediated activation by *Ef*Avs5. *Ef*Avs5 proteins form active filaments via SIR2 and NOD self-association, with sensor-mediated clustering enhancing their organization, allowing the NAD^+ depletion during phage infection. Moreover, the inactive NOD of *Ef*Avs5 requires ATP binding for its defensive role, whereas high ATP concentration impedes its NADase activity.

Result

1. *Ef*Avs5 consumes NAD^+ to confer defense

Avs5 system is widely distributed across Gram-negative phyla, especially Pseudomonadota (Fig. S1). To define the molecular anti-phage defense mechanism of Avs5, we investigated a single protein Avs5 defense system from *E. fergusonii* phage-inducible chromosomal islands (PICI), named *Ef*Avs5 (Fig. 1A). *Ef*Avs5 is reported to defense against diverse *Escherichia coli*, *Salmonella* and *Klebsiella pneumoniae* phages[13]. We cultured *E. coli* cells expressing *Ef*Avs5 and found protection against T7 phages. The C terminal of *Ef*Avs5 is supposed to sense the phage invasion, while the SIR2 domain is suggested to be the effector depleting NAD^+. Indeed, a single amino acid substitution at NADase active site (N141A) was sufficient to abolish phage defense by the *Ef*Avs5 system, confirming that the NADase activity is essential for defense. Similarly, a point mutation disrupting the NOD active site, K379A in walker A or D426A in walker B, as well as a deletion of the C-terminal sensor domain, also abolished defense (Fig. 1A).

Growth curves of *E. coli* cultures in the presence of *Ef*Avs5 kept growing when subjected to the low (0.2) or medium (2) multiplicity of infection (MOI) in contrast to the cells expressing N141A mutant or lacking *Ef*Avs5 (Fig. 1B). We measured the survival rate of cells infected with T7 and found that *Ef*Avs5 increased cell survival after the first infection cycle (about 20 minutes) (Fig. 1C). Further analysis showed that the phages amplified rapidly in the infected cells lacking *Ef*Avs5, but not in the presence of *Ef*Avs5 (Fig. 1D). To investigate the effector's activity during immunity, we detected the cellular NAD^+ content after infection with T7 phage. When subjected to the T7 phage infection, compared to cells lacking *Ef*Avs5, the concentration of NAD^+ in the *Ef*Avs5-expressing cells was declining rapidly after the first infection cycle, and began to rise in the second infection cycle (Fig. 1E). These results suggest that *Ef*Avs5 consumes NAD^+ to effectively prevent phage amplification and leads to the population-level protection.

2. Architecture of *Ef*Avs5 filament assembly

To biochemically characterize the Avs5 system, we purified *Ef*Avs5 protein overexpressed in *E. coli* BL21(DE3). The freshly isolated *Ef*Avs5 exists as soluble monomer (Fig. S2). Cryo-EM imaging of the monomer *Ef*Avs5 revealed small particles. We tried to resolve the structure but only obtained two-dimensional (2D) classes in poor resolution, possibly due to the flexibility (Fig. S3). However, the purified *Ef*Avs5 becomes visibly cloudy after stored at 4°C or -80°C for two weeks. Negative staining analysis of the suspension of *Ef*Avs5 confirmed that a significant fraction of the particles (>50%) exhibited bundled 8-nm-wide fibrous assembly, and some of them extending up to ~400 nm in length (Fig. 2A). Bundled fibrils can be connected parallelly or end-to-end and extend up to several micrometers. Since previous studies show that the activated SIR2 or Toll/interleukin-1 receptor (TIR) can assemble into helical filaments in Thoeris defense system, TIR-STING and TIR-SAVED effector, respectively[11,14,15], we quantified the NADase activity of *Ef*Avs5. The freshly purified *Ef*Avs5 was deficient in the NADase activity, but the filamentous *Ef*Avs5 displayed robust NADase activity (Fig. 2B).

To gain more insight into the filament formation, we determined the cryo-electron microscopy (cryo-EM) structure of the active *Ef*Avs5. The final cryo-EM map was reconstructed using a total of 228,053 single particles and refined to a nominal resolution of 3.4 Å, with approximately 2.8 Å at the center of filament and approximately 6.8 Å at the peripheral sensor lobes (Fig. 2C, Fig. S4 and Table S1). The model was built with eight *Ef*Avs5 molecules assembled into a helical filament, and extra densities suggest unlimited entries of both ends. The repeating building block of the filament is *Ef*Avs5 dimer with a C_2 symmetry arranged into a regular helical structure with a helical twist of 84.531° and a helical rise of 48.600 Å (Fig. 2C). The filament is held together by 2 sets of inter-subunit interactions, one between subunit n and n+3 and the other between subunit n+1 and n+2 (Fig. 2D). The *Ef*Avs5 proteins fold into five domains: a catalytic SIR2 domain, a core NOD, which comprises the nucleotide-binding domain (NBD), helical domain (HD) and wing-helical domain (WHD) and the C-terminal sensor domain (Fig. 1A and Fig. 2E). The core of the helix is composed of the SIR2 and the NOD domain, whereas the C-terminal domain

is pointing away and not involved in the helical contacts (Fig. 2E).

3. The dimerization of *Ef*Avs5

In the *Ef*Avs5 filament, the individual dimeric unit adopts a C_2 symmetric conformation with a tight interface (2329.2 $Å^2$ of buried surface area) (Fig. 3A). Within each *Ef*Avs5 dimer unit, abundant contacts are observed between the WHD of one subunit and the NBD of its adjacent subunit, encompassing salt bridges and hydrogen bonds, revealing an oligomerization pattern distinct from other characterized active STAND ATPases, which primarily oligomerize through NBD-NBD and WHD-WHD interactions (Fig. S5). The NBD of the n subunit interacts with the WHD of the n+1 subunit, comprising the salt bridge of the K461(n)- E589(n+1), K473(n)- E580(n+1), and the hydrogen bonds of the T474(n)-Y583/R570(n+1) (Fig. 3B). Meanwhile, the WHD of the n subunit interacts with the NBD of the n+1 subunit using slightly different residues, comprising the specific contacts of the E580(n)- H362(n+1), and the hydrogen bonds of the Y583(n)- T474(n+1). The dimeric interface is expanded by additional hydrogen bonds between its N-terminal SIR2 domains (Fig. 3C). To probe the role of the dimer formation in *Ef*Avs5 activity, we generated mutants of the dimeric interface. The substitutions of Y241 and T262 in SIR2 domain, H362A and K461 in NOD abolished *Ef*Avs5 system antiviral defense, indicating that dimer formation is obligatory for *Ef*Avs5 anti-phage activity *in vivo* (Fig. 3D).

4. SIR2- and NOD-dependent filamentation

The *Ef*Avs5 structure features both SIR2 and NOD engaging in intra- and inter-dimer interactions, resulting in two spirals: one dominated by SIR2, the other by NOD (Fig. 4A, B and E). The SIR2 domain within *Ef*Avs5 system exhibits a typical two-domain fold (Fig. 4D), resembling DSR2(PDB ID: 8WYB, rmsd of 1.160 Å for 74 aligned Cα atoms) and ThsA (PDB ID: 8BTO, rmsd of 1.247 Å for 84 aligned Cα atoms)[11,12], except for a longer α3 creating a broader substrate channel (Fig. S6). The large domain (LD) has a Rossmann-fold core that is conserved among all the SIR2 proteins, while the small domain (SD) lacks the three-stranded zinc-binding motif compared to human Sirt5[16].

The interface between SIR2 dimers is non-parallel to the helical axis (Fig. 4A), burying ~1218.8 $Å^2$ of surface area (Fig. 4B). SIR2 α4, α10 and α12 helices contribute to the intra-dimer interactions (Fig. 3C), whereas the loop connecting β3 and β4 forms polar interactions and hydrogen bonds with the loop between β4 and α9 of the adjacent SIR2, thereby constituting the inter-dimer interactions and facilitating the assembly of *Ef*Avs5 filaments (Fig. 4C). Interestingly, despite the similarity of the structure, the oligomerization mechanism of *Ef*Avs5-SIR2 is different from SIR2-HerA, ThsA and DSR2 (Fig. S7). Identical to the intra-dimer interaction, the inter-dimer interactions of NOD also mainly include the NBD-WHD contacts, but adopt a different mechanism (Fig. 4E). The NBD interface of the n+1 molecule is predominantly negatively charged (I303, E307, E404), complementing the positively charged interface of WHD domain of n+2 molecule (K552, H622, K623) (Fig. 4F and G).

To probe the role of the filament formation in *Ef*Avs5 activity, we generated mutants D164A

and R185A of the interface between n and n+3 subunits, and double mutants I303A/E307A, E404A/K552A and H622A/K623A of the interface between n+1 and n+2 subunits. These substitutions abolished *Ef*Avs5 system antiviral defense, indicating that both SIR2-based and NOD-based filament formation is obligatory for *Ef*Avs5 anti-phage activity *in vivo* (Fig. 3D).

5. NADase catalytic pocket

As expected, modeling of NAD^+ within the active site in the cryo-EM map of *Ef*Avs5 was not feasible due to degradation by the active SIR2. Superimposing the SIR2 domain of *Ef*Avs5 onto both the active and inactive conformations of ThsA reveals a comparable active pocket, situated within the SIR2 dimer (Fig. 5A and Fig. 2D). Dimerization likely contributes to the stabilization of the active pocket. In the case of ThsA and DSR2, the position of the loop above the active pocket decides to block the NAD^+ access to the active site or enable NAD^+ binding, thus control the NADase activity of SIR2[11,17]. However, in the *Ef*Avs5, the longer α3 pull this loop far away the active pocket (Fig. 5A and Fig. S6), indicating a different activation mechanism adopted by *Ef*Avs5. In the *Ef*Avs5-NAD^+ predicted model, the A41, T140, N141, Y142, N180, Y202, S233 in the pocket interact with NAD^+, creating an ideal condition for the reaction (Fig. 5B). The Y202 is also involved in SIR2-based dimerization. These residues are highly conserved in the bacterial SIR2 proteins, except the substitution of an Asn residue with His at residue 180 in *Ef*Avs5 (Fig. S8).

6. ATP inhibits the NADase activity of the *Ef*Avs5 system

The NOD of *Ef*Avs5 is an AAA^+ ATPase, belongs to a novel STAND NTPase 3 family found in bacterial conflict systems and in metazoan TRADD-N associated counter-invader proteins[18]. The structural comparison in Dali server[19] suggested that *Ef*Avs5's NOD is most similar to the plant NLR RPP1(PDB ID: 7CRC, rmsd of 1.160 Å for 56 aligned Cα atoms) and cell death protein 4 in *Caenorhabditis elegans* (PDB ID: 4M9S, rmsd of 1.239 Å for 45 aligned Cα atoms). Notably, we found that *Ef*Avs5 is an inactive ATPase either in the monomer or filament assembly (Fig. 5C). Consistently, the cryo-EM map allows modelling of ATP molecules in each NOD active site (Fig. 5D), although we did not add additional ATP during the sample preparation. In the structure, ATP molecules are buried in the active pocket between NBD and WHD (Fig. 5E), with an adjacent magnesium ion coordinated by the canonical Walker A and B motif (Fig. 5F). The K379 and S380 in Walker A form hydrogen bonds with the oxygens of the phosphate groups, determining the orientation of ATP. Meanwhile, the acidic D426 in Walker B binds to the Mg^{2+}. The recognition of the γ-phosphate group of ATP in the ZAR1 resistosome and Apaf-1 apoptosome is facilitated by an arginine residue in the conserved 'TT/SR' motif, which is crucial for their activation and preserved as 'TTR' and R453 in *Ef*Avs5[20,21]. The I351 forms hydrogen bonds with the N6 atoms of the adenine ring (Fig. 5F). The region spanning residues 300-366, sometimes described as the fish-specific NACHT-associated (FISNA) domain, resembles the active state of NLRP3 (PDB ID:8EJ4), triggering conformational alterations and oligomerization[22]. The accurate positioning of ATP is crucial for the functionality of the *Ef*Avs5 system, as evidenced by the phage plaque assays with WalkerA/B mutants (Fig. 1A). The deficiency

221 of ATP hydrolysis probably results from its WHD domain's unique conformations near the
222 active site, particularly the hydrogen bonding between R537 and the ATP phosphate,
223 contrasting with other active STAND ATPases (Fig. 5F and Fig. S9).
224
225 Based on the role of ATPase in sustaining *Ef*Avs5's activity *in vivo*, we investigated the
226 potential impact of ATP on NAD^+ hydrolysis. Our findings revealed that low ATP
227 concentrations (0.05 and 0.5 mM) had negligible effects, whereas 5 mM ATP significantly
228 reduced *Ef*Avs5's NADase activity by 40% (Fig. S10). Notably, GTP and dGTP also
229 effectively inhibited NADase activity, while other NTPs/dNTPs showed minimal effects,
230 except for a slight inhibition by UTP (Fig. 5G). These results indicate that specific
231 NTP/dNTP and its concentration can inhibit *Ef*Avs5's NADase activities.
232
233 **7. Filamentous cluster formation mediates *Ef*Avs5 anti-phage activity**
234 *Ef*Avs5 filaments are organized into higher-order structures, forming bundles or three-
235 dimensional networks (Fig. 2A). Although density maps of the filament bundle were not
236 available, interactions between filaments were observed during 2D classification in cryo-
237 EM analysis (Fig. 6A), in which the *Ef*Avs5 exhibits an end-to-end linkage between dimers
238 from adjacent filaments (Fig. 6B). Notably, the C-terminal sensor possesses a
239 predominantly positive charge, which complements the negatively charged interface of the
240 N-terminal SIR2 domain residing in adjacent filaments (Figure 6C). These interactions
241 would enable the *Ef*Avs5 filament to extend in four distinct directions, thereby promoting
242 the formation of parallel bundles (Figure 6D). The C-terminus of *Ef*Avs5 does not
243 participate in the formation of the individual filament but may play a crucial role in filament
244 clustering. Deletion of the entire C-terminal sensor abolished *Ef*Avs5 activity (Fig. 1A).
245 Further analysis confirmed that deletion of C-terminal six positively charged amino acids
246 similarly abolished *Ef*Avs5's resistance to phage invasion, as well as the mutations of D79A,
247 E85A and K792A at interaction interfaces (Fig. 6E). These results indicated that filament
248 clustering may be essential for the anti-phage function of *Ef*Avs5.
249
250 **Discussion**
251 In this study, we determined the cryo-EM structures of the *Ef*Avs5 and found that *Ef*Avs5
252 assembles into bundled filaments for NADase activity and anti-phage defense. We propose
253 the following model for *Ef*Avs5 (Fig. 6F). Without phage infection, *Ef*Avs5 adopts an
254 inactive, monomeric conformation in cells. Phage infection triggers *Ef*Avs5 to form filament
255 bundles, in which SIR2 adopts a dimeric active state. This active state enables *Ef*Avs5 to
256 rapidly degrade NAD^+, leading to an abortive infection that prevents propagation of phage
257 through a population of cells.
258
259 The *Ef*Avs5 structure displays a filament assembly distinct from the characterized SIR2-
260 containing defense systems and STAND proteins, underlining the universal yet diverse
261 nature of filamentation as an antiviral mechanism across prokaryotic and eukaryotic
262 immune systems. The *Ef*Avs5 filament is formed by *Ef*Avs5 dimers with a C2 symmetry
263 arranged into a high-order complex, involving comprehensive SIR2-SIR2 and NBD-WHD
264 interactions. In SIR2-APAZ/Ago, DSR2, SIR2-HerA and Thoeris system, SIR2 domains

265 function as monomers, tetramers (dimer of dimers), dodecamers (hexamer of dimers) and
266 filament (spiral of tetramers), respectively[7-10]. Compared with the SIR2-based filamentation
267 in ThsA, the NOD and SIR2 domain work together to facilitate filament formation in *Ef*Avs5,
268 highlighting their independent yet complementary roles in the assembly process. Moreover,
269 to the best of our knowledge, *Ef*Avs5 represents the first STAND family protein reported to
270 assemble into functional filaments. The activation of STAND family proteins typically
271 involves oligomerization, which includes tetramers (*Se*Avs3, *Ec*Avs4, and plant TIR-NLRs),
272 pentamers (plant ZAR1), heptamers (animal apoptosome Apaf-1) or octamers (Drosophila
273 dark apoptosome)[4,21,23-25]. Notably, *Solanum lycopersicum* NRC2 (*Sl*NRC2) was recently
274 found to form filaments at elevated concentrations, but adopt an inactive conformation to
275 avoid self-activation. Distinct from *Ef*Avs5, the *Sl*NRC2 filament consists of three identical
276 protofilaments, which contain copies of tetramers[26].
277
278 The activation observed in this study appears to be correlated with the accumulation of
279 *Ef*Avs5 proteins, mirroring previous findings in plants where concentration-dependent
280 hypersensitive response cell death was mediated by the plant NLR protein[27,28].
281 Considering its genomic localization on a PICI, intracellular expression of *Ef*Avs5 may be
282 tightly regulated to avoid unnecessary activity. The phage signals activating *Ef*Avs5 remain
283 unclear. We speculated that the activation of *Ef*Avs5 upon phage infection may involve
284 binding of an as-yet-unidentified protein or compound; alternatively, it may be a response
285 to changes in substrate concentration. Firstly, *Ef*Avs5 may interact with either phage-
286 derived proteins, akin to the DSR2 system[9], or host-derived proteins, such as that involved
287 in the bNACHT25 system[29], leading to the activation of filament formation and enzymatic
288 activity. However, our attempt to identify potential activators through screening of escape
289 phages was unsuccessful. Secondly, as suggested by the finding that the binding of the
290 TIR substrates NAD^+ and ATP induces phase separation and activation of TIR *in vitro*[30],
291 one of the potential activation mechanisms of *Ef*Avs5 may be the substrate-based
292 response.
293
294 Above all, our structural and biochemical findings offer insights into the molecular
295 mechanism of Avs5 bacterial immune system, highlighting the conservation of
296 oligomerization as a key regulatory mechanism governing antiviral defense across
297 prokaryotes and metazoans.
298
299 **Limitations of the study**
300 Our findings elucidate the fundamental mechanisms underlying *Ef*Avs5 function, yet the
301 activation signals associated with phage infection remain elusive and warrant further
302 investigation. Apart from biochemical assays on mutants, our results lack direct evidence
303 of *Ef*Avs5 forming fibrillar clusters *in vivo*. Additionally, we propose that ATP intricately
304 modulates *Ef*Avs5 activity, but the underlying molecular mechanisms require detailed
305 clarification.
306
307 **Acknowledgements**
308 This work was supported by National Natural Science Foundation of China (32370071,

32070040), National Key Research and Development Program of China (2020YFA0907900, 2019YFA0905400).
We thank the staff members of the Electron Microscopy System at the National Facility for Protein Science in Shanghai (NFPS), Shanghai Advanced Research Institute, Chinese Academy of Sciences, China for providing technical support and assistance in data collection. We thank Jing Liu, Xinqiu Guo and Mengyu Yan at the Instrument Analysis Center (IAC) of Shanghai Jiao Tong University for providing assistance in data collection.

Author contributions

J.Z. and Y.W. designed the experiments and analyzed data.
Y.W. and Y.T. performed biochemical assays.
Y.W. and X.Y. conducted cryo-EM data collection.
Y.W. conducted image processing, atomic model, building and refinement and structural analyses.
Y.W. and Y.F performed bioinformatics analysis.
Y.W. and J.Z. wrote the manuscript.

Declaration of interests

The authors declare no competing interests.

Data availability

The atomic coordinates have been deposited in the Protein Data Bank under accession codes 9JAP. The corresponding maps have been deposited in the Electron Microscopy Data Bank under the accession number EMD-61299.

Supplemental information

Document S1. Figures S1–S10 and Table S1-S2

STAR Methods

Plasmid construction

DNA fragments encoding *Ef*Avs5 from *Escherichia fergusonii* PICI EfCIRHB19-C05 (QML19490.1) were synthesized and inserted into the expressing plasmids pET28a with N-terminal His_6-tag by Universe Gene Technology (Tianjin). The DNA fragments encoding *Ef*Avs5 was subcloned into the pBAD33 vector for phage infection assays. Plasmids carrying *Ef*Avs5 mutants were constructed using site-directed mutagenesis. Primers used are listed in Table S2.

Protein expression and purification

The vector pET28a-*Ef*Avs5 was transformed into *E. coli* BL21(DE3). Induction of expression was achieved by adding 0.3 mM isopropyl-β-D-thiogalactopyranoside (IPTG) and incubated for 16 h at 16°C and 220 rpm. The cells were then harvested and resuspended in buffer A (50 mM Tris, pH 8.0, 500 mM NaCl, 5 mM $MgCl_2$, 10% glycerol, 1 mM β-mercaptoethanol and 5 mM imidazole). After purification by nickel-NTA, the eluate was further loaded onto a size exclusion chromatography column (SEC) (Superose 6,

353 Cytiva) equilibrated with buffer B (20 mM Tris, pH 8.0, 150 mM NaCl, 5 mM $MgCl_2$, 5%
354 glycerol) and the purified proteins were stored at −80 °C.
355
356 **Plaque assays**
357 *E. coli* MG1655 possessing pBAD33- *Ef*Avs5, its mutants or an empty vector(pBAD33)
358 were grown at 37℃ in LB medium. When the OD_{600} reached 0.4, cells were induced with
359 0.5% L-arabinose for 1 hour. Then, 150 μL of the culture was mixed with 3 mL LB containing
360 0.8% low-melting agarose（with 0.5% L-arabinose added）, and the mixture was poured
361 into LB agar base layer in the 9 cm petri dish. Ten-fold dilutions of high-titers(>10^8pfu/mL)
362 of phage T7 were spotted onto the agar and incubated overnight at 37 ℃. The next day,
363 plates were photographed with blue-white light reflection in the dark box.
364
365 **Phage-infection in liquid medium**
366 *E. coli* MG1655 possessing pBAD33- *Ef*Avs5, its mutant(N141A) or an empty
367 vector(pBAD33) were grown until the OD_{600} reached 0.4. These cultures were then induced
368 with 0.5% L-arabinose for 1 hour, and diluted in LB containing 0.5% L-arabinose to an OD
369 of ~0.1. Phage T7 was added to the culture at final MOI of 0.02, 0.2, 2, and 10.
370 Subsequently, 200 μL of the diluted culture was placed into the wells of a 96-well plate.
371 During shaking, the OD_{600} was measured every 5 minutes at 37℃ for 6 hours.
372
373 **Cell survival assays**
374 Overnight cultures of *E. coli* MG1655, either containing the plasmid pBAD33-*Ef*Avs5 or an
375 empty vector, were diluted 1:100 into fresh LB medium. These cultures were grown at 37°C
376 with the addition of 0.5% L-arabinose until they reached an OD_{600} of 0.4. Subsequently,
377 the cells were harvested by centrifugation, washed with LB, and resuspended to an OD_{600}
378 of 0.2. To each sample, phage T7 was added at an MOI of 5, while control samples were
379 left without phage addition. Following a 20-minute adsorption period, serial 10-fold dilutions
380 of each sample were plated onto LB agar, and the plates were incubated overnight at 37°C.
381 The cell survival rate was determined by comparing the CFU obtained from the samples
382 with phage T7 addition to the CFU obtained from the control samples without phage,
383 expressed as a percentage.
384
385 **Phage burst size measurements**
386 Overnight cultures of *E. coli* MG1655 harboring either the pBAD33-*Ef*Avs5 plasmid or an
387 empty vector were diluted 1:100 in LB medium supplemented with 0.5% L-arabinose.
388 These diluted cultures were then grown at 37°C until they reached an OD_{600} of 0.4.
389 Subsequently, T7 phages were introduced to the cultures at an MOI of 0.1, and the infection
390 process was allowed to proceed at 37°C. To establish a baseline for the initial phage titer,
391 an equal volume of phage was added to LB media and used as the reference for time 0 of
392 infection. After infection for 20, 40, and 60 minutes at 37°C, which represent approximately
393 one, two, and three cycles of T7 phage replication, respectively, 0.5 mL samples of the
394 culture were withdrawn. These samples were centrifuged at 5000 rpm for 7 minutes and
395 the supernatants were filtered through a 0.22 μm filter. The titer of the T7 phages present
396 in the filtered supernatants was determined by a plaque assay using *E. coli* MG1655 as

397 the host.
398
399 **NAD(H) degradation measurements**
400 NAD(H) concentrations were measured using the Innochem Coenzyme I NAD(H) Content
401 Assay Kit (WST colorimetry), following the manufacturer's instructions. Briefly, overnight
402 cultures were diluted 1:100 in 50 mL LB with 0.5% L-arabinose, grown to OD_{600} of 0.4, and
403 infected with T7 phage at an MOI of 2. At indicated times, 1 mL cultures were centrifuged,
404 resuspended in acidic extract, sonicated, boiled, rapid cooled, and centrifuged.
405 Supernatant was neutralized with alkaline extract. 50 μL of the neutralized supernatant
406 was combined sequentially with 250 μL of Reagent 1, 75 μL of Reagent 2, 150 μL of
407 Reagent 3, and 35 μL of Reagent 4 in the determination tube. After a 1-hour dark reaction,
408 Reagent 5 was added to the mixture. In the control tube, Reagent 5 was added first,
409 followed by the supernatant, maintaining identical steps thereafter. Absorbance was
410 measured at 450 nm, and NAD(H) levels were calculated using a standard curve and
411 normalized to the amount of NAD(H) present in an equivalent volume of sample with an
412 OD_{600} of 0.1 to allow for accurate comparisons between samples.
413
414 **Negative staining analysis**
415 The *Ef*Avs5 sample was directly applied to a glow-discharged 400-mesh Cu grid (Beijing
416 ZhongJingKeYi Technology) for 30 s. After side blotting, the grid was immediately stained
417 with 2% uranyl formate and then blotted again from the side. Staining was repeated twice
418 with a 30 s incubation with uranyl formate in the final staining step. EM images were
419 collected on a Talos F200C G2 at a nominal magnification of 52,000× and at a defocus of
420 about 5 μm.
421
422 **Cryo-EM grid preparation and data acquisition**
423 3.5 μL of the *Ef*Avs5 samples were added to freshly glow-discharged Quantifoil R1.2/1.3
424 Cu 300 mesh grids. In a Vitrobot (FEI, Inc.), grids were plunge-frozen in liquid ethane after
425 being blotted for 2 s at 16°C with 100% chamber humidity. The grids were imaged using
426 EPU on Titan Krios 300 kV microscopes with a K3 detector. Totally 4318 movies were
427 collected under the defocus ranged from −0.8 to −1.6 μm, and the magnification was 81k
428 in super-resolution mode. 32 frames per movie were collected with a total dose of 40 $e^{-}/Å^{2}$.
429
430 **Cryo-EM data processing and model building**
431 The cryo-EM data was processed using CryoSPARC suite v4.5.3[31]. After motion correction,
432 patch CTF estimation and manual exposure curation, 1425 movies were selected. The first
433 set of particles was picked using a filament tracer, and after two-dimensional (2D)
434 classification, good templates were selected for template picking. A total of 1,392,237
435 particles were picked using a template picker and extracted (box size 360 pixels) from
436 1,425 accepted micrographs (Fig. S4). Two rounds of 2D classification were conducted
437 and 364,551 particles were picked and used for ab-initio reconstruction (three classes).
438 The largest 3D class (228,053 particles, 62.6%) was selected and refined by homogeneous
439 refinement, non-uniform refinement and CTF refinement to give the final map (global
440 resolution, 3.44 Å). Helical parameters (helical twist and helical rise) were determined by

441 helical refinement job. The initial model of *Ef*Avs5 wes generated by AlphaFold[32]. The
442 model of ATP was built in Coot[33]. The models of *Ef*Avs5 were fitted into the cryo-EM density
443 maps using ChimeraX[34]. The model was refined in Coot and Phenix with secondary
444 structure, rotamer and Ramachandran restraints[35]. The Map versus Model FSCs was
445 generated by Phenix (Fig. S4). The statistics of cryo-EM data processing and refinement
446 were listed in Table S1.
447
448 ***In vitro* NADase activity**
449 The *Ef*Avs5 NADase activity was evaluated through an εNAD^+-based fluorescence assay,
450 wherein the enzymatic cleavage of the nicotinamide glycosidic bond in εNAD^+ results in
451 the formation of εADPR, which subsequently emits a fluorescent signal. In a 96-well black
452 flat-bottom plate, 100 μL reaction mixtures were prepared, each containing 50 μM of εNAD^+
453 (Sigma catalogue No. N2630) and 0.5 μM *Ef*Avs5 proteins in reaction buffer (20 mM Tris,
454 pH 8.0, 150 mM NaCl, and 5% glycerol, with and without the addition of nucleotides). A
455 mixture containing only the reaction buffer and εNAD^+ was used as a control. The reactions
456 were then loaded into a BioTek Synergy H1 microplate reader, and fluorescence intensities
457 were recorded at 37°C every 20 seconds for 15 minutes, employing excitation and
458 emission wavelengths of 310 nm and 410 nm, respectively. All experiments were
459 conducted in triplicate to ensure reproducibility.
460
461 **ATPase activity**
462 ATPase activities were evaluated by using Malachite Green Phosphate Detection Kit
463 (Beyotime). Each 200 μL reaction mixture consisted of 5μM *Ef*Avs5 proteins in a reaction
464 buffer (20 mM Tris, pH 8.0, 150 mM NaCl, 5 mM $MgCl_2$ and 0.5 mM ATP). A mixture without
465 the addition of *Ef*Avs5 proteins served as a control. Following a 30-minute incubation at
466 37°C, 70 μL of color reagent was added and the mixture was further incubated for another
467 30 minutes. Subsequently, the absorbance at 620 nm was measured using a multi-
468 detection microplate reader (Tecan Spark). Phosphate levels were then calculated using a
469 standard curve generated with phosphate standards. All experiments were conducted in
470 triplicate to ensure reproducibility.
471
472 **Phylogenetic analysis of Avs5 systems**
473 The coding sequence of Avs5 was acquired from two sources: firstly, by utilizing the
474 defense finder tool to scan through all bacterial and archaeal genomes housed in the IMG
475 (Integrated Microbial Genomes & Microbiomes) database from November 2023, aiming to
476 identify proteins that encode the Avs5 system[36]; secondly, by leveraging the Foldseek
477 search server to discover proteins (leveraging AlphaFold/UniProt50, ensuring a coverage
478 exceeding 80%) that exhibited a high degree of structural similarity to Avs5[37]. To eliminate
479 redundancy, MMseqs was employed with the specified parameters '–min-seq-id 0.90' and
480 '-c 0.8', resulting in 263 filtered sequences[38]. These sequences were subsequently aligned
481 using MAFFT, with the parameters set to '--maxiterate 1000 –globalpair' for optimal
482 alignment[39]. Following alignment, trimAl was applied to refine the alignment by trimming
483 unnecessary regions[40]. The phylogenetic tree was then constructed using IQ-TREE,
484 incorporating the parameters '-nstop 500 -bb 1000 -m LG+F+I+G4' for enhanced accuracy

485 and robustness[41]. Finally, iTOL was utilized for the visualization and annotation of the
486 phylogenetic tree[42].
487
488
489 **References**

490 1 Millman, A. *et al.* An expanded arsenal of immune systems that protect bacteria from
491 phages. *Cell Host & Microbe* **30**, 1556-1569.e1555 (2022).
492 https://doi.org:10.1016/j.chom.2022.09.017
493 2 Vassallo, C. N., Doering, C. R., Littlehale, M. L., Teodoro, G. I. C. & Laub, M. T. A
494 functional selection reveals previously undetected anti-phage defence systems in the
495 E. coli pangenome. *Nature Microbiology* **7**, 1568-1579 (2022).
496 https://doi.org:10.1038/s41564-022-01219-4
497 3 Gao, L. *et al.* Diverse enzymatic activities mediate antiviral immunity in prokaryotes.
498 *Science* **369**, 1077-1084 (2020). https://doi.org:10.1126/science.aba0372
499 4 Gao, L. A. *et al.* Prokaryotic innate immunity through pattern recognition of conserved
500 viral proteins. *Science* **377** (2022). https://doi.org:10.1126/science.abm4096
501 5 Dorstyn, L., Akey, C. W. & Kumar, S. New insights into apoptosome structure and
502 function. *Cell Death Differ* **25**, 1194-1208 (2018). https://doi.org:10.1038/s41418-017-
503 0025-z
504 6 Huang, S. *et al.* NLR signaling in plants: from resistosomes to second messengers.
505 *Trends in Biochemical Sciences* **48**, 776-787 (2023).
506 https://doi.org:10.1016/j.tibs.2023.06.002
507 7 Koopal, B. *et al.* Short prokaryotic Argonaute systems trigger cell death upon detection
508 of invading DNA. *Cell* **185**, 1471-1486.e1419 (2022).
509 https://doi.org:10.1016/j.cell.2022.03.012
510 8 Ka, D., Oh, H., Park, E., Kim, J.-H. & Bae, E. Structural and functional evidence of
511 bacterial antiphage protection by Thoeris defense system via NAD+ degradation.
512 *Nature Communications* **11** (2020). https://doi.org:10.1038/s41467-020-16703-w
513 9 Garb, J. *et al.* Multiple phage resistance systems inhibit infection via SIR2-dependent
514 NAD+ depletion. *Nature Microbiology* **7**, 1849-1856 (2022).
515 https://doi.org:10.1038/s41564-022-01207-8
516 10 Tang, D. *et al.* Multiple enzymatic activities of a Sir2-HerA system cooperate for anti-
517 phage defense. *Molecular Cell* **83**, 4600-4613.e4606 (2023).
518 https://doi.org:10.1016/j.molcel.2023.11.010
519 11 Tamulaitiene, G. *et al.* Activation of Thoeris antiviral system via SIR2 effector filament
520 assembly. *Nature* (2024). https://doi.org:10.1038/s41586-024-07092-x
521 12 Yang, X., Wang, Y. & Zheng, J. Structural insights into autoinhibition and activation of
522 defense-associated sirtuin protein. *Int J Biol Macromol* **277**, 134145 (2024).
523 https://doi.org:10.1016/j.ijbiomac.2024.134145
524 13 Fillol-Salom, A. *et al.* Bacteriophages benefit from mobilizing pathogenicity islands
525 encoding immune systems against competitors. *Cell* **185**, 3248-3262.e3220 (2022).
526 https://doi.org:10.1016/j.cell.2022.07.014
527 14 Morehouse, B. R. *et al.* Cryo-EM structure of an active bacterial TIR–STING filament
528 complex. *Nature* **608**, 803-807 (2022). https://doi.org:10.1038/s41586-022-04999-1

529 15 Hogrel, G. *et al.* Cyclic nucleotide-induced helical structure activates a TIR immune
530 effector. *Nature* **608**, 808-812 (2022). https://doi.org:10.1038/s41586-022-05070-9
531 16 Du, J. *et al.* Sirt5 is a NAD-dependent protein lysine demalonylase and desuccinylase.
532 *Science* **334**, 806-809 (2011). https://doi.org:10.1126/science.1207861
533 17 Yin, H. *et al.* Insights into the modulation of bacterial NADase activity by phage proteins.
534 *Nature Communications* **15** (2024). https://doi.org:10.1038/s41467-024-47030-z
535 18 Kaur, G., Iyer, L. M., Burroughs, A. M. & Aravind, L. Bacterial death and TRADD-N
536 domains help define novel apoptosis and immunity mechanisms shared by prokaryotes
537 and metazoans. *Elife* **10** (2021). https://doi.org:10.7554/eLife.70394
538 19 Holm, L. Dali server: structural unification of protein families. *Nucleic Acids Res* **50**,
539 W210-w215 (2022). https://doi.org:10.1093/nar/gkac387
540 20 Wang, J. *et al.* Reconstitution and structure of a plant NLR resistosome conferring
541 immunity. *Science* **364** (2019). https://doi.org:10.1126/science.aav5870
542 21 Zhou, M. *et al.* Atomic structure of the apoptosome: mechanism of cytochrome c- and
543 dATP-mediated activation of Apaf-1. *Genes Dev* **29**, 2349-2361 (2015).
544 https://doi.org:10.1101/gad.272278.115
545 22 Xiao, L., Magupalli, V. G. & Wu, H. Cryo-EM structures of the active NLRP3
546 inflammasome disc. *Nature* **613**, 595-600 (2023). https://doi.org:10.1038/s41586-022-
547 05570-8
548 23 Ma, S. *et al.* Direct pathogen-induced assembly of an NLR immune receptor complex
549 to form a holoenzyme. *Science* **370** (2020). https://doi.org:10.1126/science.abe3069
550 24 Wang, J. *et al.* Reconstitution and structure of a plant NLR resistosome conferring
551 immunity. *Science* **364** (2019). https://doi.org:10.1126/science.aav5870
552 25 Pang, Y. *et al.* Structure of the apoptosome: mechanistic insights into activation of an
553 initiator caspase from Drosophila. *Genes Dev* **29**, 277-287 (2015).
554 https://doi.org:10.1101/gad.255877.114
555 26 Ma, S. *et al.* Oligomerization-mediated autoinhibition and cofactor binding of a plant
556 NLR. *Nature* **632**, 869-876 (2024). https://doi.org:10.1038/s41586-024-07668-7
557 27 Zhang, Y., Dorey, S., Swiderski, M. & Jones, J. D. Expression of RPS4 in tobacco
558 induces an AvrRps4-independent HR that requires EDS1, SGT1 and HSP90. *Plant J*
559 **40**, 213-224 (2004). https://doi.org:10.1111/j.1365-313X.2004.02201.x
560 28 Horsefield, S. *et al.* NAD(+) cleavage activity by animal and plant TIR domains in cell
561 death pathways. *Science* **365**, 793-799 (2019).
562 https://doi.org:10.1126/science.aax1911
563 29 Conte, A. N. *et al.* (2024). https://doi.org:10.1101/2024.06.04.597415
564 30 Song, W. *et al.* Substrate-induced condensation activates plant TIR domain proteins.
565 *Nature* **627**, 847-853 (2024). https://doi.org:10.1038/s41586-024-07183-9
566 31 Punjani, A., Rubinstein, J. L., Fleet, D. J. & Brubaker, M. A. cryoSPARC: algorithms for
567 rapid unsupervised cryo-EM structure determination. *Nat Methods* **14**, 290-296 (2017).
568 https://doi.org:10.1038/nmeth.4169
569 32 Jumper, J. *et al.* Highly accurate protein structure prediction with AlphaFold. *Nature*
570 **596**, 583-589 (2021). https://doi.org:10.1038/s41586-021-03819-2
571 33 Casanal, A., Lohkamp, B. & Emsley, P. Current developments in Coot for
572 macromolecular model building of Electron Cryo-microscopy and Crystallographic Data.

Protein Sci **29**, 1069-1078 (2020). https://doi.org:10.1002/pro.3791

34 Pettersen, E. F. *et al.* UCSF ChimeraX: Structure visualization for researchers, educators, and developers. *Protein Sci* **30**, 70-82 (2021). https://doi.org:10.1002/pro.3943

35 Liebschner, D. *et al.* Macromolecular structure determination using X-rays, neutrons and electrons: recent developments in Phenix. *Acta Crystallogr D Struct Biol* **75**, 861-877 (2019). https://doi.org:10.1107/S2059798319011471

36 Tesson, F. *et al.* Systematic and quantitative view of the antiviral arsenal of prokaryotes. *Nat Commun* **13**, 2561 (2022). https://doi.org:10.1038/s41467-022-30269-9

37 van Kempen, M. *et al.* Fast and accurate protein structure search with Foldseek. *Nat Biotechnol* **42**, 243-246 (2024). https://doi.org:10.1038/s41587-023-01773-0

38 Steinegger, M. & Söding, J. MMseqs2 enables sensitive protein sequence searching for the analysis of massive data sets. *Nat Biotechnol* **35**, 1026-1028 (2017). https://doi.org:10.1038/nbt.3988

39 Katoh, K., Rozewicki, J. & Yamada, K. D. MAFFT online service: multiple sequence alignment, interactive sequence choice and visualization. *Brief Bioinform* **20**, 1160-1166 (2019). https://doi.org:10.1093/bib/bbx108

40 Capella-Gutiérrez, S., Silla-Martínez, J. M. & Gabaldón, T. trimAl: a tool for automated alignment trimming in large-scale phylogenetic analyses. *Bioinformatics* **25**, 1972-1973 (2009). https://doi.org:10.1093/bioinformatics/btp348

41 Nguyen, L. T., Schmidt, H. A., von Haeseler, A. & Minh, B. Q. IQ-TREE: a fast and effective stochastic algorithm for estimating maximum-likelihood phylogenies. *Mol Biol Evol* **32**, 268-274 (2015). https://doi.org:10.1093/molbev/msu300

42 Letunic, I. & Bork, P. Interactive Tree Of Life (iTOL) v5: an online tool for phylogenetic tree display and annotation. *Nucleic Acids Res* **49**, W293-w296 (2021). https://doi.org:10.1093/nar/gkab301

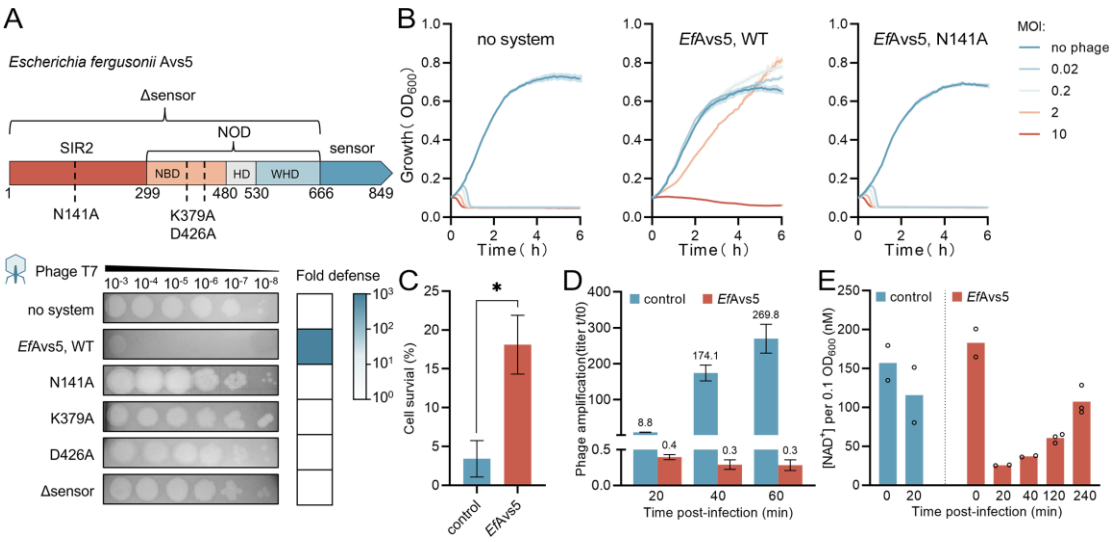

Fig. 1. *Ef*Avs5 consumes NAD⁺ to confer defense.

(**A**) Domain organization of the *Ef*Avs5 protein from *Escherichia fergusonii* and efficiency of plating of T7 phages infecting *E. coli* expressing *Ef*Avs5 or an empty vector. Data are representative images of n=3 biological replicates. Mutations used are indicated below the domain organization. NBD, nucleotide-binding domain; HD, helical domain; WHD, wing-helical domain; NOD, nucleotide-binding oligomerization domain. (**B**) Infection time courses for liquid cultures of *E. coli*, with *Ef*Avs5, *Ef*Avs5 N141A or empty vector, infected at different multiplicities of infection (MOI) of phage T7. Data represent the mean of three replicates and shaded regions represent the standard error of the mean (SEM). (**C**) Survival of *E. coli* cells expressing either the *Ef*Avs5 or empty vector as a control infected at an MOI of 5 with T7 for 20 minutes. Data represent the mean of three replicates and error bars represent the SEM. (**D**) Titer of T7 phage propagated on *E. coli* cells expressing either the *Ef*Avs5 or empty vector as a control infected at an MOI of 0.1 with T7. Data represent the titer of T7 measured in PFU/mL after indicated time from initial infection, divided by the original phage titer prior to infection. Data represent the mean of three replicates and error bars represent the SEM. (**E**) Measurement of NAD^+ concentration in *E. coli* expressing *Ef*Avs5 or empty vector as a control at the indicated time points after infection with phage T7 at an MOI of 2, normalized to an OD_{600} of 0.1. The control group underwent near-complete lysis after 20 minutes of infection, precluding the quantification of NAD^+ content. Data represent the mean of two or three replicates and error bars represent the SEM.

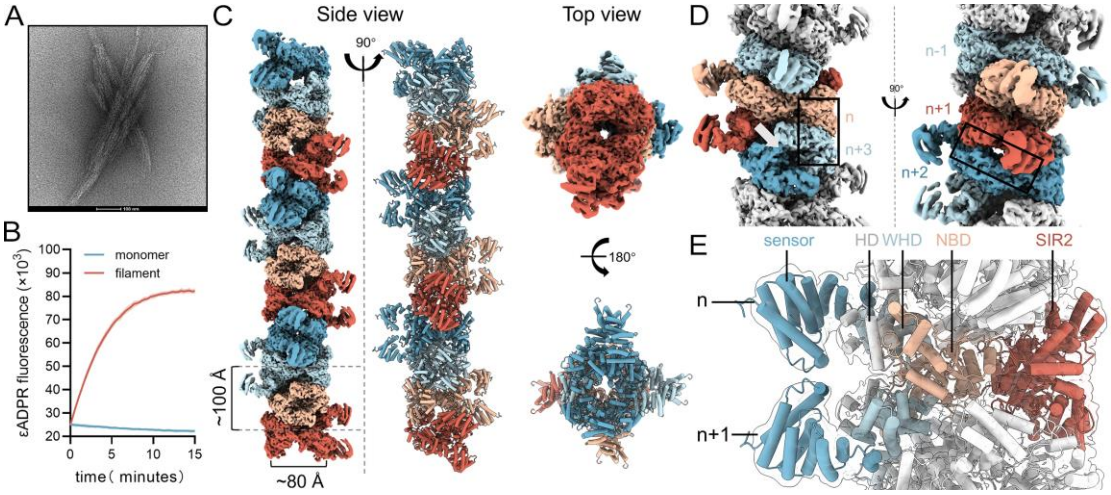

Fig2. Cryo-EM structure of the *Ef*Avs5 filament.

(**A**) Representative negative-stain micrograph images of *Ef*Avs5. The scale bar represents 100 nm. (**B**) *Ef*Avs5's NADase activity is activated by filamentation. After the addition of ε-NAD^+, total fluorescence was measured over time. Data represent the mean of three replicates and shaded regions represent the SEM. (**C**) Top and side views of the density map and the atomic model of *Ef*Avs5 filament. (**D**) Detailed view of *Ef*Avs5 filament to show the subunit interfaces. Two interfaces are indicated with boxes, and the NAD^+ active site is indicated with a grey arrow. (**E**) The core of *Ef*Avs5 filament is composed of the SIR2 domain and the NOD.

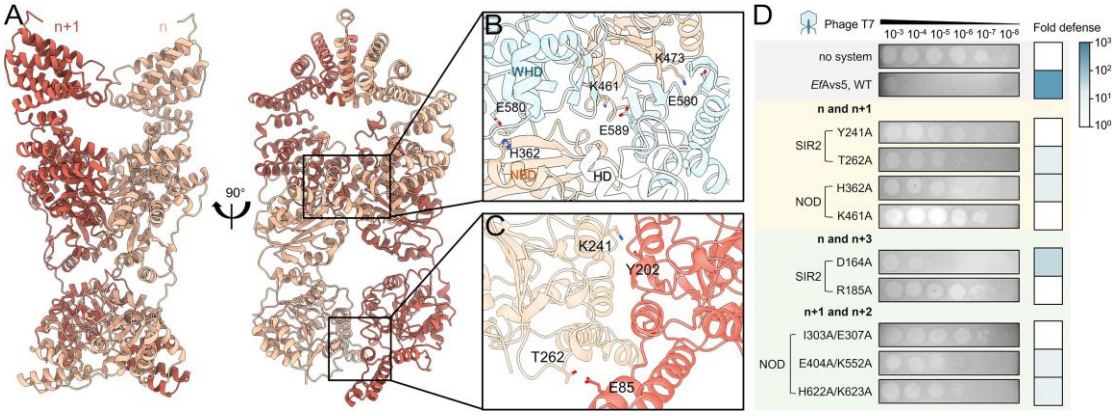

Fig3. The mechanism of *Ef*Avs5 dimerization.

(**A**) The structure of the *Ef*Avs5 dimer. (**B**) Details of the NOD-based dimeric interfaces. (**C**) Details of the SIR2-based dimeric interfaces. (**D**) Phage plaque assay of *E. coli* expressing *Ef*Avs5 variants with mutations at the interfaces. The yellow background highlights the intra-dimer interactions, while the green background indicates the inter-dimer interactions. Data are representative images of n=3 biological replicates.

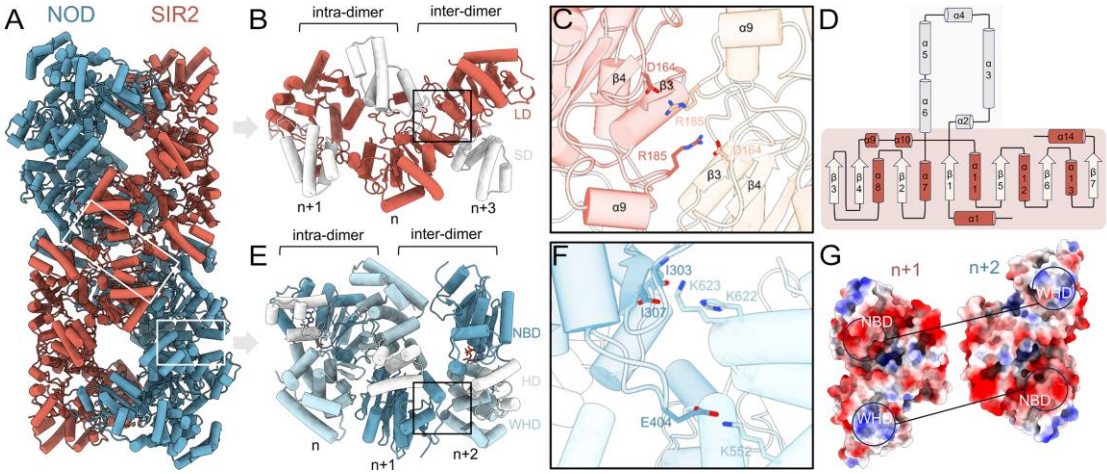

Fig 4. SIR2- and NOD-dependent filamentation.

(**A**)Two spirals dominated by NOD (blue) and SIR2 domains (red), respectively. The C-terminal domains of *Ef*Avs5 are hided. The inter-dimer interactions are indicated by white boxes. (**B**) The intra-dimer and inter-dimer interface of SIR2 domain of the n+1, n, n+3 subunits. LD, large domain; SD, small domain. (**C**) Detailed inter-dimer interface of SIR2 domain. The n, n+3 subunits of *Ef*Avs5 was colored red and orange, respectively. (**D**) SIR2 topology diagrams of *Ef*Avs5. The small domain is shaded grey, and the large domain is shaded red. (**E**) The intra-dimer and inter-dimer interface of NOD domain of the n, n+1, n+2 subunits. (**F**) Detailed inter-dimer interface of NOD domain. The NBD of n+1 subunit, and the WHD of n+2 subunit of *Ef*Avs5 were colored dark and light blue, respectively. (**G**) The electrostatic potential inter-dimer interface of two adjacent NOD domains.

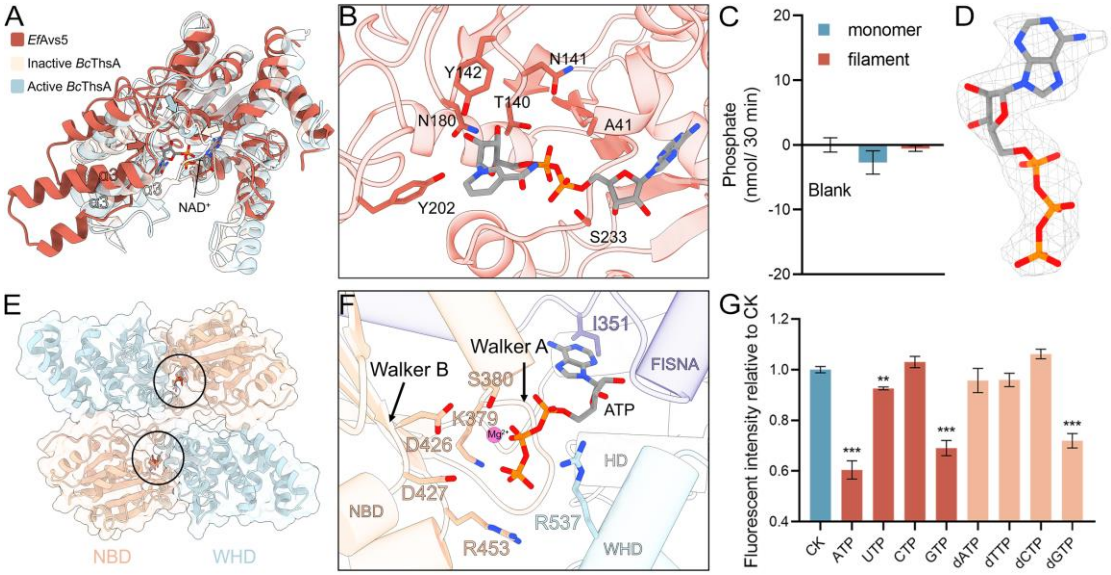

Fig 5. The NAD⁺ hydrolyzing pocket and ATP binding pocket of *Ef*Avs5.

(**A**) Overlay of SIR2 domain (red) of *Ef*Avs5 with the inactive (6LHX, light orange) and activated (light blue) *Bc*ThsA SIR2 domains. NAD^+ from the activated ThsA (1ICI) is shown. The loops above the NAD^+ pocket of *Ef*Avs5 and ThsA SIR2 are indicated by arrows colored as in the color scheme. (**B**) Residues of *Ef*Avs5 interacting with NAD^+ molecule highlighted in sticks in the predicted *Ef*Avs5-NAD^+ binding model. (**C**)ATPase activity assay of the monomer or the filament *Ef*Avs5. Data represent the mean of three replicates and error bars represent the SEM. (**D**) Cryo-EM map of ATP. (**E**) The binding pocket of ATP in the NOD dimer. (**F**) Residues of *Ef*Avs5 coordinating ATP molecule highlighted in sticks. The highly conserved Walker A motif and Walker B motif were indicated by arrows. (**G**) Effects of NTPs and dNTPs (5 mM) on NADase activity of the *Ef*Avs5. CK: no NTPs/dNTPs added. Data represent the mean of three replicates and error bars represent the SEM.

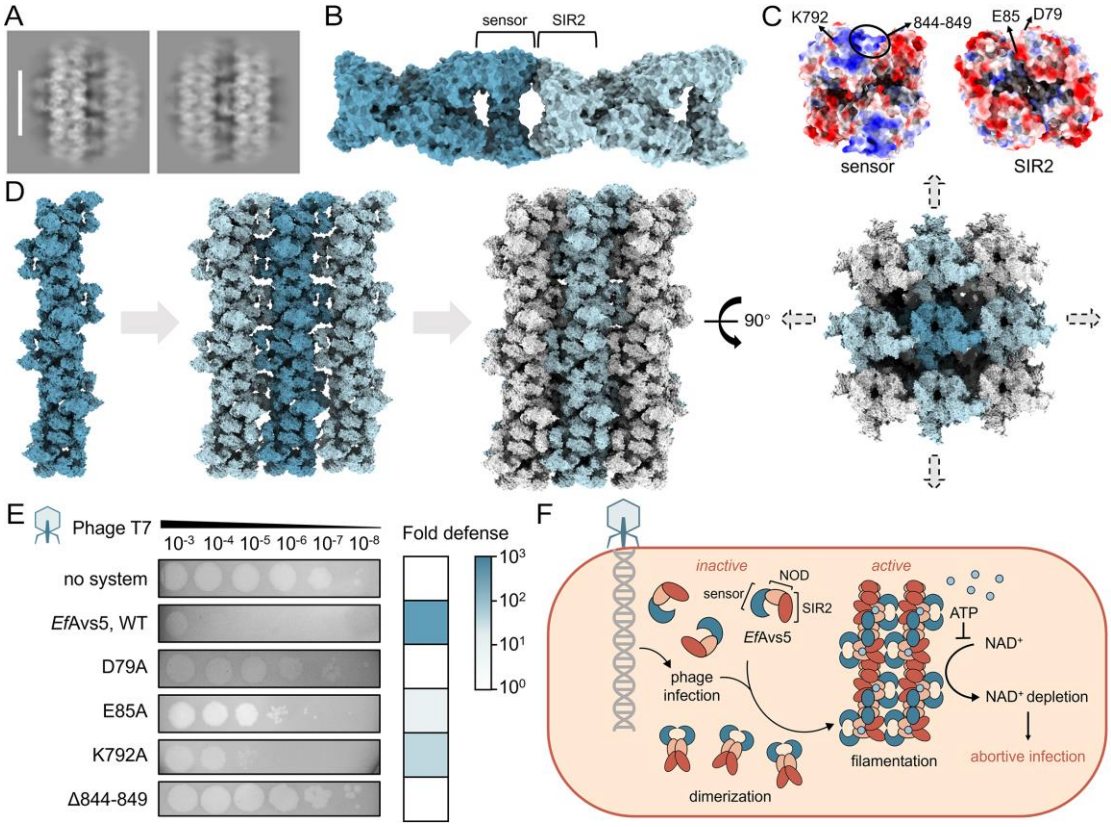

Fig 6. Filamentous cluster formation mediates *Ef*Avs5 anti-phage activity

(**A**) 2D class averages of the particle stacks, showing the bundled filament assembly. The scale bar represents 130 Å. (**B**) Interacting *Ef*Avs5 dimers in adjacent filaments. (**C**) The electrostatic potential interface of C-terminal sensor and N-terminal SIR2 domain. (**D**) A schematic diagram of the filament cluster assembly of *Ef*Avs5. (**E**) Phage plaque assay of *E. coli* expressing *Ef*Avs5 variants with mutations at the clustering interfaces. Data are representative images of n=3 biological replicates. (**F**) Proposed model of *Ef*Avs5 immune mechanism. Without phage infection, *Ef*Avs5 remains inactive as monomer. Phage infection activates *Ef*Avs5, forming filament bundles where SIR2 enable rapid NAD^+ degradation and aborting phage infection.